PAPER • OPEN ACCESS

Nesting BiVO$_4$ nanoislands in ZnO nanodendrites by two-step electrodeposition for efficient solar water splitting

To cite this article: Ali Can Güler *et al* 2024 *J. Phys. D: Appl. Phys.* **57** 355110

View the article online for updates and enhancements.

The Electrochemical Society
Advancing solid state & electrochemical science & technology

ECS UNITED

247th ECS Meeting
Montréal, Canada
May 18-22, 2025
Palais des Congrès de Montréal

Abstracts due December 6th

Showcase your science!

Nesting BiVO$_4$ nanoislands in ZnO nanodendrites by two-step electrodeposition for efficient solar water splitting

Ali Can Güler[1]**, Jan Antoš**[1]**, Milan Masař**[1]**, Michal Urbánek**[1]**, Michal Machovský**[1]**, Rajesh Dagupati**[2]**, Michal Žitňan**[2]**, José J Velázquez**[2]**, Dušan Galusek**[2,3] **and Ivo Kuřitka**[1,4,*] (ID)

[1] Centre of Polymer Systems, Tomas Bata University in Zlin, Tr. T. Bati 5678, 760 01 Zlin, Czech Republic
[2] Centre for Functional and Surface Functionalized Glass, Alexander Dubček University of Trenčín, Študentská 2, SK-911 50 Trenčín, Slovakia
[3] Join Glass Centre of the IIC SAS, TnU AD, and FChPT STU, Trenčín, Slovakia
[4] Department of Chemistry, Faculty of Technology, Tomas Bata University in Zlín, Vavrečkova 5669, 760 01 Zlín, Czech Republic

E-mail: kuritka@utb.cz, guler@utb.cz, antos@utb.cz, masar@utb.cz, murbanek@utb.cz, machovsky@utb.cz, rajesh.dagupati@tnuni.sk, michal.zitnan@tnuni.sk, jose.velazquez@tnuni.sk and dusan.galusek@tnuni.sk

CrossMark

Abstract

Photoanodes with a large electrochemically active surface area, rapid charge transfer, and broadband light harvesting capacity are required to maximize the photoelectrochemical (PEC) water splitting performance. To address these features, we demonstrate that 3D hierarchal ZnO nanodendrites (NDs) can be sensitized with BiVO$_4$ nanoislands by chemical and thermal treatments of electrodeposited Bi metal films. The flat band measurements and optical characterization suggested that the resulting heterojunction had type-II band alignment with a viable charge transfer from BiVO$_4$ to ZnO NDs. In parallel, PL analysis revealed inhibition of the charge recombination rate by the electron transfer between BiVO$_4$ and ZnO NDs. Upon AM 1.5 G illumination, BiVO$_4$/ZnO NDs heterojunction yielded the highest photocurrent efficiency (0.15 mA·cm^{-2} at 1.2 V vs. NHE), which was attributed to its enhanced surface area (due to the presence of small dendrite branches), extended broadband light absorption extending from UV to visible light regions, and the most efficient interfacial charge transfer as proven by electrochemical impedance spectroscopy (EIS) studies. Besides, the incident photon-to-current conversion efficiency and applied bias photon-to-current efficiency tests confirmed an improved spectral photoresponse of the heterojunction based photoanode, particularly towards the visible light spectrum. The results outline a promising synthesis route for building heterojunctions between visible light active and wide band gap semiconductors for the use as a highly efficient photoanodes in a PEC cell.

* Author to whom any correspondence should be addressed.

J. Phys. D: Appl. Phys. **57** (2024) 355110

A C Güler *et al*

1. Introduction

Solar energy conversion to chemical energy (i.e. hydrogen) using semiconducting materials via photoelectrochemical (PEC) water splitting has been regarded as efficient sustainable energy technology since the pioneering demonstration by Honda and Fujishima [1, 2]. The overpotential for water oxidation (oxygen evolution reaction (OER)) and water reduction (hydrogen evolution reaction (HER)) in this process is partially compensated by the photoinduced voltage of the light absorber [3, 4]. The semiconductor must hence possess an appropriate band alignment with the water redox potentials. The OER and HER could be driven by the PEC water splitting at potentials below 1.23 V and above 0 V with reference to the reversible hydrogen electrode (RHE), respectively [5]. The important argument affecting the solar-to-hydrogen conversion efficiency (STH) are light absorption, charge separation/transport and surface catalytic reaction (charge transfer) [6, 7].

Many properties of semiconductor nanorods (NRs) can be significantly altered when their radial dimension (diameter) is equal or below the characteristic length of the interesting solid state phenomena such as the exciton Bohr radius, exciton diffusion length, wavelength of irradiation and phonon mean free path [8, 9]. For instance, Song *et al* fabricated a composite titania thin film composed of quasi-aligned rutile NRs embedded in anatase aggregates and its PEC behavior was significantly enhanced [10]. Recently, more efforts have been devoted on constructing three-dimensional (3D) hierarchical nanostructures from low-dimensional subunits. Compared to 1D morphologies, 3D complex zinc oxide (ZnO) morphologies present a larger active surface area, which results in a more rapid charge transfer process and water oxidation kinetics [11, 12]. This hierarchical structural design can increase the number of light transport paths and thereby improve light harvesting capacity [13, 14]. ZnO nanodendrites (NDs) included in this class of nanostructures are very promising candidate for solar energy conversion applications due to their low-cost and a facile synthesis process. In contrast to the conventional methods in which 3D ZnO NDs are grown over sequentially reseeded ZnO NRs surface in aqueous phase [15–17], Wu *et al* purposed an alternative fabrication method utilizing a supersaturated solution without any sequential seed layer or organic structure-directing agent [18]. Nevertheless, besides all other assets, a wide band gap (∼3.2 eV) of ZnO is considered as the fundamental obstacle to achieving moderate STH efficiency via its utilization in the PEC water splitting. A novel material design is therefore needed to influence the factors mentioned above.

Photosensitization with a narrow band gap semiconductor has emerged as an effective means of extension of the optical activity of ZnO NDs into the visible region. Among the different photosensitizers that show photoactivity under visible light, monoclinic bismuth vanadate (BiVO₄) was chosen as the light absorber due to its the suitable band gap (∼2.4 eV), appreciable band edge positions for water oxidation and the matched band structure with that of ZnO [19, 20]. The monoclinic BiVO₄ alone demonstrated photocatalytic activity for the O₂ evolution from an aqueous silver nitrate solution under visible light irradiation [21, 22]. It was also reported that the formation of heterojunction photoanode between the wurtzite ZnO and monoclinic BiVO₄ promotes the charge separation and transport of electrons and holes assisted by the built-in electric field at the interface and light absorption at a wider wavelength range (UV and vis), which then boosts the PEC performance [23, 24].

In this sense, Yan *et al* reported the fabrication of ZnO NRs/BiVO₄ heterojunction through chemical bath deposition followed by successive ionic layer deposition [25]. They observed that photocurrent of ZnO NRs/BiVO₄ (1.72 mA·cm⁻² at 1.2 V vs. Ag/AgCl) was higher than that of ZnO NRs photoanode at the same potential. The improvement in photoconversion was associated with the extended spectral response towards the visible spectrum and lower recombination rate of photogenerated charge carrier. Moniz *et al* successfully synthesized 1D ZnO coupled with nanoparticulate BiVO₄ and cobalt phosphate (Co–Pi) as a hole acceptor [26]. They found that Co–Pi/BiVO₄/ZnO exhibited 12-fold increase in photocurrent (∼3 mA·cm⁻²) compared to the BiVO₄. The enhancement results from higher light absorption, electron flow from BiVO₄ to ZnO, and hole transfer to Co-Pi for favorable OER. Recently, Yang and Wu constructed novel Co–Pi/BiVO₄/ZnO NDs photoanode based on metal organic deposition of BiVO₄ on the surface of hydrothermally grown ZnO NRs [27]. The resultant electrode yielded an optimized photocurrent density of 3.5 mA·cm⁻² at 1.23 V vs. RHE after being fully depleted at a low bias potential (0.8 V vs. RHE). Along with the superior light harvesting capability and charge injection efficiency by co-catalyst Co–Pi, the authors claimed that fully depleted junction originating from thin BiVO₄ shells led to better charge transport, which in turn enhanced the PEC activity. However, synthesis techniques available to produce nanoporous morphology electrodes are quite limited. Kim and Choi presented electrochemically deposited nanoporous BiVO₄ from bismuth oxyiodide (BiOI) on fluorine-doped tin oxide substrates [28]. They suggested that the voids between 2D crystal structure of BiOI allowed the deposition of ultra-thin plates (∼20 nm) by inhibiting the grain formation of

J. Phys. D: Appl. Phys. **57** (2024) 355110

A C Güler *et al*

$BiVO_4$ during the conversion process. Kang *et al* demonstrated that the electrodeposited Bi dendritic electrodes followed by the introduction of a V precursor solution during the oxidation process can lead to $BiVO_4$ NPs. The resultant $BiVO_4$ thin film had a high surface area and a good electrical continuity among the particles [29]. Using the similar electrodeposition procedure, Bai *et al* fabricated $Cu_2O/BiVO_4$ p–n heterojunction photoanode and obtained the maximum photocurrent density of 1.72 mA·cm^{-2} (1.23 V vs RHE), which is 4.5 times higher than that of pristine $BiVO_4$ thin film (~0.38 mA·cm^{-2}) at the same applied potential [30].

In view of the advantages mentioned above, herein, we introduce a facile strategy for the construction of $BiVO_4/ZnO$ NDs heterojunction photoanode with a novel nanostructure for PEC water splitting. The branches with the lengths of 300–400 nm were directly formed on hydrothermally grown primary ZnO NRs with a diameter of 84 nm in the absence of any seed layer or organic structure directing agent to produce ZnO NDs. $BiVO_4$ nanoislands nested in ZnO NDs were prepared by electrodeposition of Bi film followed by the introduction of V solution and thermal treatment. A two-step electrodeposition procedure generated an intimate contact at the interface between the constituent semiconductors. $BiVO_4/ZnO$ NDs heterojunction was identified to have staggered band arrangement (type II), leading to an efficient photogenerated electron–hole separation and rapid interfacial charge transfer. Under AM 1.5 G illumination, the heterojunction photoanode achieved a higher PEC performance than the $BiVO_4$, ZnO NDs, and ZnO NRs photoelectrodes prepared in this study. This new approach may pave the way for rational design of heterojunctions between narrow band gap and wide band gap semiconductors with optimal structure and compositions.

2. Experimental section

2.1. Preparation of ZnO NDs photoanode

The ZnO NR arrays were synthesized by hydrothermal method. Initially, 0.8 M zinc acetate dihydrate $(Zn(CH_3CO_2)_2.2H_2O$, Penta) and 0.8 M diethanolamine $((CH_2CH_2OH)_2NH$, CDH Fine Chemicals) were dissolved in isopropanol $((CH_3)_2CHOH$, Microchem), and stirred at 50 °C for 1 h. After an overnight aging, the sol was spin-coated on cleaned indium tin oxide coated (ITO, 5–15 Ω sq^{-1}, Sigma Aldrich) glass substrates at 3000 rpm for 30 s. The coated substrate was calcined in an ambient atmosphere at 400 °C for 1 h to obtain the ZnO seed layer. The typical growth solution consisting of 0.025 M zinc nitrate hexahydrate $(Zn(NO_3)_2 \cdot 6H_2O$, Sigma Aldrich), 0.025 M hexamethylenetetramine $((CH_2)_6N_4$, Lachner), and 0.5 ml polyethyleneimine (PEI, branched, average $M_w \sim 800$ by LS, Sigma Aldrich) was preheated for 2 h at 95 °C. The aged growth solution turned to yellow straw color. The seeded film with its conductive side facing downwards was immersed in the preheated solution (in yellow straw color) and kept at 95 °C for 6 h.

The branches of ZnO NDs were formed directly on the ZnO NRs without any assistance from another seeds and organic structure-directing agent, as described elsewhere [31]. The ZnO NRs grown on ITO substrate were first immersed into an aqueous solution of 0.057 M zinc acetate dihydrate and 0.5 M sodium hydroxide (NaOH, Lachner) for 20 min at room temperature. During this process, the etch pits formed that served as growth centers for the formation of nanocactus (NCs), which then turned into branches after 1 h growing at 100 °C for in the same solution. The obtained ZnO NDs were carefully rinsed with deionized water and dried at 60 °C.

It should be mentioned that branch development only started from a supersaturated solution in a metastable state at a high concentration of NaOH. The supersaturation of zinc acetate and NaOH solution can be reached before the solution turns opaque after ~5 min at room temperature. Therefore, it is very important to immerse ZnO NRs in a clear solution before precipitation. A more detailed information can be found where it was primarily observed [18].

2.2. Preparation of BiVO₄ and BiVO₄/ZnO NDs photoanodes

Scheme 1 presents the synthesis procedure to prepare ZnO NDs coated with $BiVO_4$ NPs, which could be converted from electrodeposited Bi metal using a modified version of the previously described chemical and thermal treatments [29]. In the first step, the plating solution was prepared by dissolving 20 mM of bismuth(III) nitrate pentahydrate $(Bi(NO)_3.5H_2O$, Sigma Aldrich) in 100 ml ethylene glycol $(HOCH_2CH_2OH$, Sigma Aldrich) solution. The deposition was achieved by passing ~0.033 C cm^{-2} at −1 V against the Ag/AgCl electrode. The other details of Bi metal electrodeposition are given in the supplementary information (figure 1S). Following that, 100 μl of dimethyl sulfoxide (DMSO, Sigma Aldrich) containing 150 mM ammonium monovanadate $(NH_4VO_3$, Sigma Aldrich) was drop-casted onto the entire Bi film (area = 2 cm^2) as the second step. The V precursor-incorporated film was calcined at 500 °C for 2 h in air. By thermal treatment, Bi and VO^{2+} oxidized to Bi_2O_3 and V_2O_5, which reacted to form $BiVO_4$. Any residual vanadium pentaoxide (V_2O_5) on the electrode was removed by soaking it in 0.125 M NaOH solution for 30 s. The resultant pure $BiVO_4/ZnO$ NDs photoanode was thoroughly washed by deionized water, and dried at 60 °C. For synthesis of $BiVO_4$, all the deposition conditions were the same, except for ITO substrates used as scaffolds.

2.3. PEC measurements

The PEC performance tests of $BiVO_4$ sensitized ZnO NDs were performed in three-electrode configuration within a plastic cuvette under front-side illumination at 87.5 mW·cm^{-2} light intensity from a Pico^{TM} solar simulator (G2V Optics) with a standard AM 1.5 G filter. The incident light in UV and visible regions (350–800 nm) is attenuated by 10% (data not shown) while passing throughout the PEC cell cuvette filled with electrolyte solution, corresponding that the light intensity at the sample surface was 78.75 mW·cm^{-2}. 0.5 M Na_2SO_4 (pH 7) was used as an electrolyte solution that was

J. Phys. D: Appl. Phys. **57** (2024) 355110

A C Güler *et al*
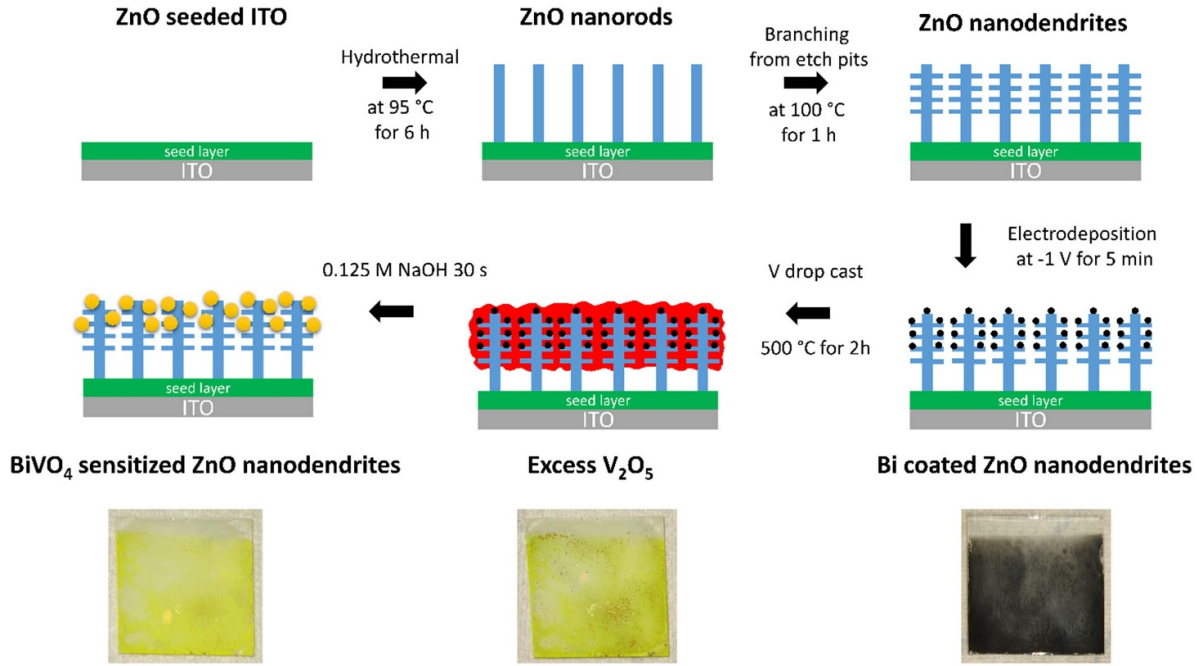
Scheme 1. Schematic representation for the fabrication of BiVO₄/ZnO NDs heterojunction photoanode.

degassed by nitrogen for 10 min to remove any dissolved oxygen before the PEC measurements. The fabricated electrodes with a fixed surface area of 0.32 cm², Pt foil and Ag/AgCl (saturated with KCl) were used as the working, counter, and reference electrodes, respectively. The potentials measured vs. Ag/AgCl electrode ($E_{Ag/AgCl}$) were converted to normal hydrogen electrode (NHE) potentials (E_{NHE}) by using the equation:

$$E_{NHE} = E_{Ag/AgCl} + 0.2 \text{ V}. \tag{1}$$

In linear sweep voltammograms, LSV (J-V), the scan rate was 20 mV s⁻¹ and the scan range was 0 V–1.5 V (vs. Ag/AgCl) both under dark and illuminated conditions. The incident photon-to-current conversion efficiency (IPCE) tests were also carried out in the three-electrode setup using 12 monochromatic channels of the solar simulator (Pico™ with AM 1.5 G filter) as the light source. The IPCE was calculated using the following equation:

$$IPCE = \frac{J_{ph}(\lambda) \times 1240}{P_{mono}(\lambda) \times \lambda} \tag{2}$$

where, J_{ph} (in mA·cm⁻²) is the photocurrent density recorded under monochromatic illumination at wavelength λ (in nm), P_{mono} (in mW·cm⁻²) is the light intensity of the monochromatic source at each wavelength, the constant 1240 (hc/e in V·nm) equals to the product of Planck's constant and the speed of light divided by the charge of an electron. The applied bias photon-to-current efficiency (ABPE), analogue to the STH efficiency with no bias, was calculated by the formula:

$$ABPE = \left[\frac{J\left(mA.cm^{-2}\right) \times \left(1.229 - |V_{app}|\right)(V) \times \eta_F}{P_{total}\left(mW.cm^{-2}\right)} \right] \tag{3}$$

in which, 1.23 V is the standard state reversible potential for water splitting, V_{app} is the applied bias (measured vs. Pt), η_F is the Faradaic efficiency for hydrogen evolution ($\eta_F = 1$ in this case), and P_{total} is the intensity of the light source.

Electrochemical impedance spectroscopy (EIS) measurements were conducted in the same electrolyte and set-up as employed in the photocurrent measurements. The EIS data under illuminated condition was obtained at 10 mV amplitude of AC signal over a frequency range of 100 kHz to 0.1 Hz. The Mott–Schottky (MS) analysis was carried out in dark at 1.5 kHz with 30 potential steps.

2.4. Characterization

The crystal structure of the samples was determined by x-ray powder diffractometry (XRD, Panalytical Empyrean DY1098) with Cu Kα radiation ($\lambda = 0.15405$ nm) under 40 kV and 45 mA in steps of 0.02°. Scanning electron microscopy (SEM, Nova NanoSEM 450) was employed to study the morphology of the samples. The elemental composition of the produced heterostructure was determined through energy-dispersive x-ray spectroscopy (EDX). The microstructure of the films was monitored by transmission electron microscopy (TEM, JEM-2100Plus, Jeol). The optical characteristics of the synthesized photoanodes were acquired by a 150 mm InGaAs integrating spheres module of a UV-Vis-NIR absorption spectrometer (Lambda 1050 Perkin Elmer). The photoluminescence spectra at room temperature were obtained by fluorescence spectrophotometer (PL, Fluorolog FL3-21, Horiba) equipped with delta diode laser DD-375 1 376 nm as an excitation source. Raman spectra were collected by a micro-Raman spectrophotometer (Renishaw in Via Reflex) at the excitation wavelength

J. Phys. D: Appl. Phys. **57** (2024) 355110

A C Güler *et al*

of 532 nm. X-ray photoelectron spectroscopy (XPS, Axis Ultra DLD spectrometer, Kratos Analytical Ltd) with a monochromatized Al Kα radiation ($h\nu = 1{,}486.7$ eV), operated at 150 W (10 mA, 15 kV), was used to explore the elemental composition and oxidation states of the elements on the surface of the BiVO$_4$/ZnO NDs. The XPS spectra were obtained using an analysis area of $\sim$300 μm $\times$ 700 μm and analyzed by Casa XPS software. Electrochemical workstation (SP-200 Potentiostat, BioLogic) with EIS was utilized to test the PEC/electrochemical performance as well as interfacial charge transfer properties of the produced electrodes.

3. Results and discussion

BiVO$_4$ nanoislands nested in sequential hydrothermally grown ZnO NDs was prepared by electrodeposition of Bi film followed by the introduction of V solution and thermal treatment. The amount of the decorated BiVO$_4$ was determined based on measuring the electrode weight before and after coating. Without contribution from ITO, the weight of ZnO NDs was determined as 0.89 mg while the weight of BiVO$_4$ deposits on ZnO NDs was determined as 0.12 mg, corresponding to formation of BiVO$_4$/ZnO NDs ($\sim$13.4 wt. %) heterostructure photoanode.

The XRD spectra of the produced electrodes are shown in figure 1. The peak positions of ZnO NDs are the same as those of ZnO NRs before growing ZnO branches, which correspond to the characteristic diffraction maxima of hexagonal wurtzite structure [32]. The dominant (002) peaks in the XRD patterns of ZnO NRs as well as ZnO NDs suggest a preferential orientation along the *c*-axis normal to the substrate rather than an anisotropic orientation. In both samples, the (002) peak at 35° with the full-width half maximum of less than 0.16° confirms a high crystallinity. An interesting aspect of this prominent peak is its stronger intensity for ZnO NDs. This change is attributed to the occurrence of branches since the crystalline volume contributes to the diffraction intensity [33]. The XRD patterns of BiVO$_4$ were found to be consistent with the characteristic diffraction peaks of monoclinic scheelite [34]. It is discernible that the electrodeposition of BiVO$_4$ did not cause any considerable peak shifting or crystal phase change of ZnO NDs. All XRD patterns of BiVO$_4$/ZnO NDs are therefore assigned to the co-existence of BiVO$_4$ and ZnO phases without any undesirable impurities. Figure 2S(a) shows the XRD patterns for ITO glass and Bi metal electrodeposited ITO glass before introducing the V precursor (DMSO containing ammonium monovanadate) to form BiVO$_4$. The peak observed at 30.80° is associated with the (222) plane of ITO [35]. The peaks in the XRD pattern of Bi-deposited ITO film are indexed as the tetragonal phase of β-Bi$_2$O$_3$ [36]. The most relevant diffraction planes are labeled, and no other impurity phase was detected. The XRD results indicate that Bi metal reacts with the atmospheric oxygen to form Bi$_2$O$_3$.

The Raman spectra of the samples are shown in figure 2. The characteristic weak peak of ZnO at 438 cm^{-1} is observed in the spectra of the ZnO NDs as well as BiVO$_4$/ZnO NDs.
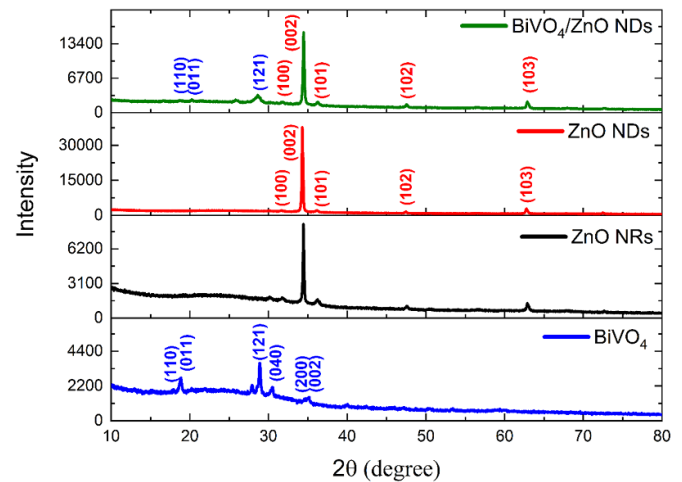

Figure 1. XRD patterns of BiVO$_4$, ZnO NRs, ZnO NDs and BiVO$_4$/ZnO NDs photoanodes.
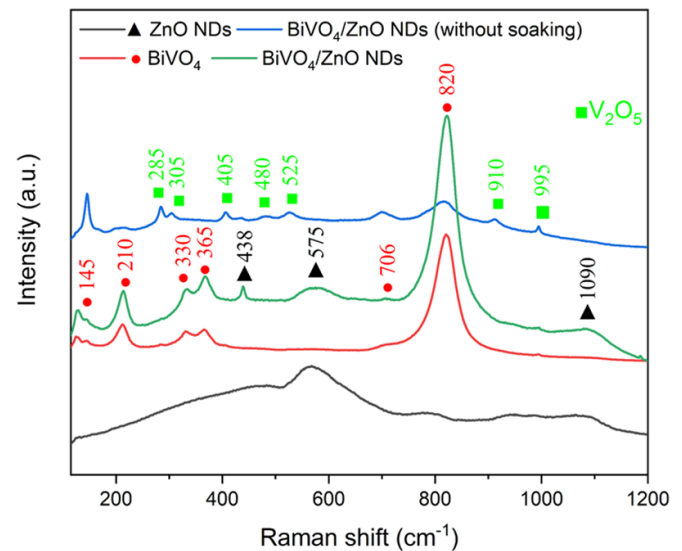
Figure 2. Raman spectra of ZnO NDs, BiVO$_4$, BiVO$_4$/ZnO NDs and BiVO$_4$/ZnO NDs without soaking in NaOH solution to remove V$_2$O$_5$.

The peaks at 1090 cm^{-1} and 575 cm^{-1} are associated with the defects in ZnO crystals [37]. On the other hand, the peaks around 820, 706, 365, 210 and 145 cm^{-1} in the Raman spectra of BiVO$_4$ and BiVO$_4$/ZnO NDs refer to monoclinic BiVO$_4$ [38], implying the formation of the crystalline BiVO$_4$ on ND ZnO structures. Raman spectral analysis was also applied to the as-prepared BiVO$_4$/ZnO NDs without soaking in NaOH solution to confirm successful removal of the residual V$_2$O$_5$. Additional vibrational modes appeared in the Raman spectra of BiVO$_4$/ZnO NDs without soaking, when compared with the Raman spectra of BiVO$_4$/ZnO NDs. Among Raman peaks of V$_2$O$_5$, the internal modes between 500–1000 cm^{-1} involve V–O stretching vibrations while the external modes between 200–500 cm^{-1} involve V–O–V bending vibrations [39]. The
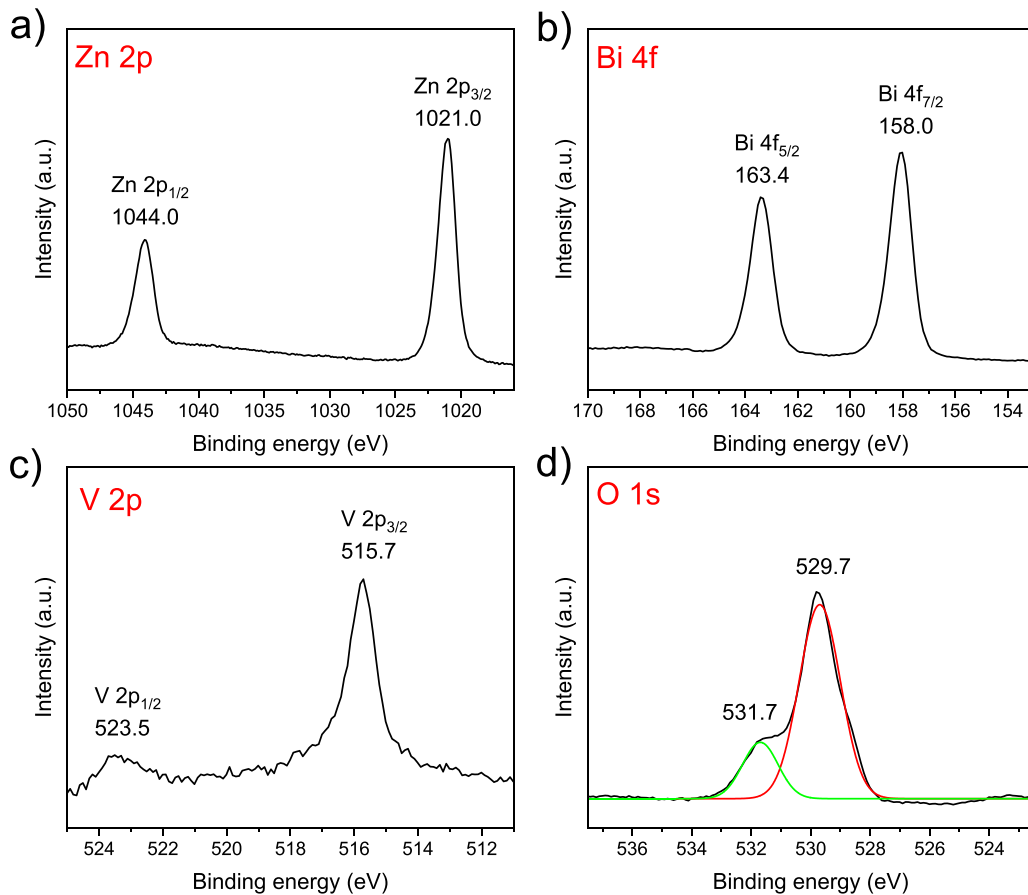
Figure 3. High resolution XPS core level spectra of $BiVO_4$/ZnO NDs (a) Zn 2p, (b) Bi 4f, (c) V 2p and (d) O 1 s.

result indicates that the excess of V_2O_5 was firmly eliminated, and pure $BiVO_4$/ZnO NDs was formed.

The composition and chemical states in a $BiVO_4$/ZnO NDs heterojunction sample was analyzed by XPS. The peak locations in all XPS spectra were corrected using C 1 s at 284.5 eV. The high resolution XPS spectrum of Zn $2p$ in figure 3(a) reveals two binding energies of 1021.0 (Zn $2p_{3/2}$) and 1044.0 (Zn $2p_{1/2}$) eV, signifying that Zn is present in the Zn^{2+} state [40]. The typical binding energies of 158.0 (Bi $4f_{7/2}$) and 163.4 (Bi $4f_{5/2}$) eV in figure 3(b) denote Bi in the 3+ state. As for the V $2p$ XPS spectrum in figure 3(c), the major peaks appeared at 515.7 (V $2p_{3/2}$) and 523.5 eV (V $2p_{1/2}$) indicate that V in $BiVO_4$/ZnO NDs photoanode is present in the oxidation state of V^{5+} [41]. Figure 3(d) demonstrates the O 1 s core level spectrum with two deconvoluted peaks at 529.7 and 531.7 eV. The peak located at 529.7 eV is mainly attributed to the lattice oxygen of ZnO crystal while the peak located at 531.7 eV is related to the hydroxyl (–OH) groups formed on the surface of specimen [42].

Cross-sectional and top-view SEM images and diameter distribution of the primarily grown ZnO NR are respectively shown in supporting information (figures 3S(a)–(c)). Growth of vertically aligned ZnO NRs on a 300 nm thick seed layer after 6 h during the hydrothermal synthesis resulted in homogeneous hexagonal arrays with a length of $\sim$2 μm and an average diameter of 44 nm. Moreover, the spines grew directly on the ZnO NRs to form the NCs at room temperature after 20 min (figure 3S(d)). As shown in figure 4(a), SEM image demonstrates that the spines developed into the branches to form ZnO NDs with high surface area after subsequent hydrothermal growth at 100 °C for 1 h. These branches lengths ranged from 300 to 400 nm. The diameter distribution of the primary ZnO NRs within NDs is shown in figure 4(b), demonstrating that the average diameter increased from 44 nm to 84 nm. It should be pointed out that the electrodeposited Bi crystals did not cover the entire ITO surface (figure 2S(b)). This island morphology of Bi is attributed to the poor dissolution of Bi deposits [28, 29]. However, as shown in figure 4(c), the ITO surface was almost fully covered with porous, uniform, and nanocrystalline $BiVO_4$. After introducing V source and after heat treatment, the morphology of $BiVO_4$ altered significantly compared to that of the original Bi metal deposits. The SEM image of $BiVO_4$/ZnO NDs heterojunction shown in figure 4(d) illustrates that electrodeposition process successfully nested $BiVO_4$ nanoislands in and on top of ZnO NDs. The size of the $BiVO_4$ nanostructures was about 200–300 nm. It should be noted that there is a difference in appearance between the growth orientation of $BiVO_4$ NPs on planar ITO and 3D complex ZnO structures. In the former, the nanoparticles accumulate laterally, in the latter, there is
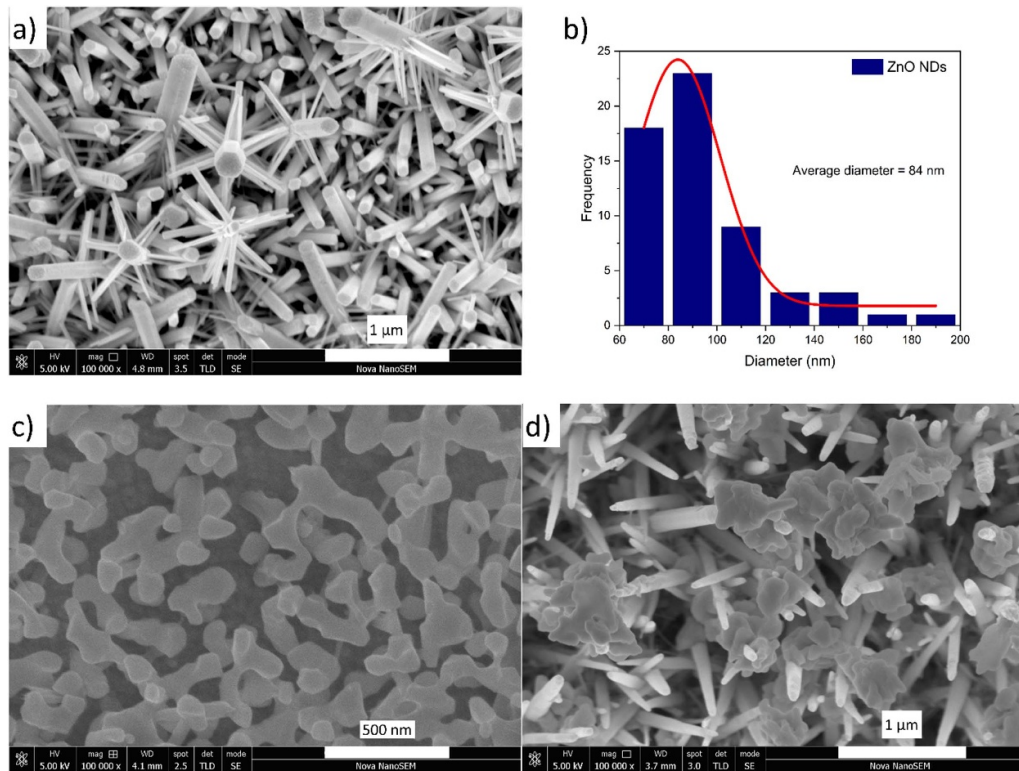
Figure 4. SEM images of (a) ZnO NDs, (b) corresponding diameter distribution of ZnO NDs, (c) BiVO$_4$, and (d) BiVO$_4$/ZnO NDs.

a vertical growth of the porous small nanoparticles stacked on top of each other appear like a single large cluster. The quality of semiconductor-semiconductor contact is essential for achieving excellent PEC performance of the heterojunction device. BiVO$_4$ nanoislands in the upper layer tightly wrap ZnO NDs and intertwine them, leading to an intimate contact at the interface for the expected good charge separation. Electrodeposition occurs on a conductive substrate by facilitating electrons for the reaction. It was reported that ZnO NRs displayed polarity dependent high electrical conductivity varying between 10.2 and 90.9 S cm^{-1} [43]. This value is much smaller than the electrical conductivity of ITO substrate that is ~10^4 S cm^{-1} [44]. Equally important is the electrical conductivity of the electrodeposited compounds. Electrons cannot easily reach all the locations at the deposits for the low conductivity phase while electrons are avaliable at all the surface sites for the high conductivity phase [45]. To emphasize again, the cathodic current during the electrodeposition of Bi metal on ZnO reached as high as -1.1 mA, signifying sufficient electrical conductivity of electrodeposited phase. Our results suggest that ZnO in the form of branched NRs provides suitable electrical and transport properties for the uniform formation of BiVO$_4$ NPs via electrodeposited Bi metal. Besides, ZnO NDs slightly corroded due to the immersion in the acidic Bi metal plating solution for 5 min.

The EDX analysis of BiVO$_4$/ZnO NDs (figure 4S) reveals that the heterostructure is only composed of zinc, bismuth, vanadium, and oxygen. The absence of any other element confirms the purity of the fabricated film.
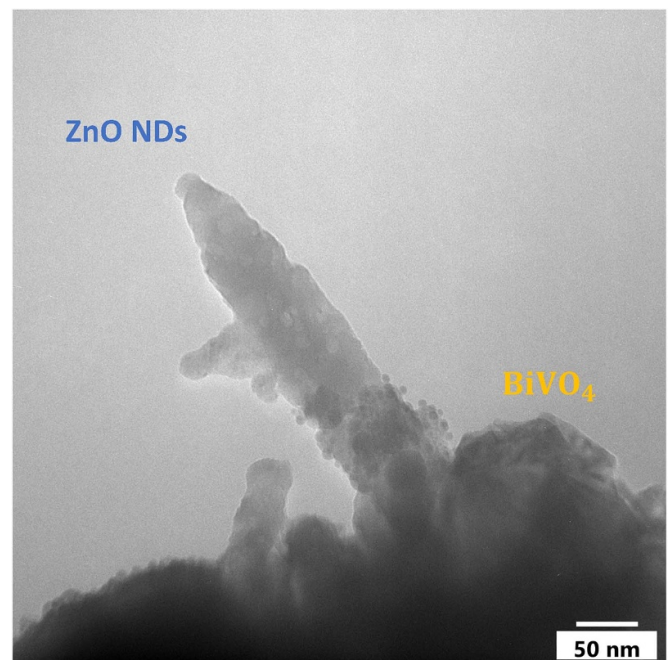
Figure 5. TEM image of BiVO$_4$/ZnO NDs heterojunction.

Figure 5 represents the TEM image of ^{BiVO}4/ZnO NDs heterostructure extracted from a large area of ND arrays. ZnO NDs slightly corroded during the electrodeposition of Bi metal film due to the acidity of the plating solution as
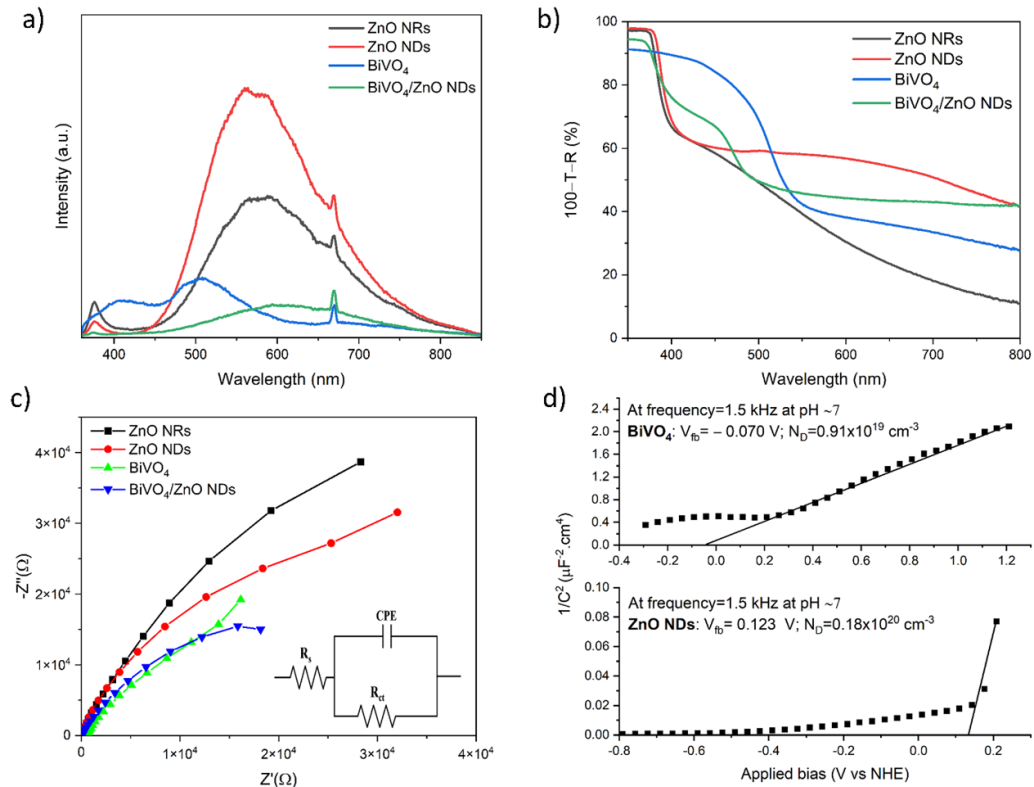
Figure 6. (a) PL spectra (excitation wavelength 335 nm, the peak at 670 nm corresponds to its second harmonics), (b) Absorption plus scattering spectra ($A + S = 100 − R − T$), (c) Nyquist plots under AM 1.5 G irradiation and (d) Mott–Schottky plot of $BiVO_4$ and ZnO NDs. semiconductors.

was also observed by SEM. The surface morphology examination indicates that a branch grew vertically from the stem of primary ZnO NRs, which have a diameter of about ∼65 nm. Moreover, the size of $BiVO_4$ crystals is about ∼200 nm with relatively darker contrast. It can also be deduced that $BiVO_4$ nanoislands are firmly bound to ZnO NDs, leading to a good electrical continuity between two phases. All these results are consistent with SEM observations.

The semiconductor heterojunction photoanode is reportedly very effective for improvement of the interfacial charge transportation and separation efficiency [23, 46]. To evaluate the recombination rate within the fabricated photoelectrodes PL measurements were performed under the excitation wavelength of 335 nm as its qualitative indication. As seen from figure 6(a), two distinctive emission peaks appeared in the PL spectra of ZnO NRs, ZnO NDs and $BiVO_4$/ZnO NDs. The peak at 376 nm results from the near band edge (NBE) transitions in ZnO [47]. Another wide and intense emission peak for the pristine ZnO samples appeared at 570 nm and was associated with the presence of the oxygen vacancies [48]. As $BiVO_4$ deposits on ZnO NDs, a red-shift of the defect-induced emission is observed at 620 nm. Annealing ZnO increases the amount of the oxygen interstitials and decreases the amount of the oxygen vacancies [49]. Therefore, this shift of visible emission could be related to the variation of the local surroundings of the defect sites as a result of annealing the heterojunction sample. In the case of $BiVO_4$, two broad peaks

at 505 and 410 nm were attributed to the NBE transition and the deep level defects, respectively [50]. In fact, high PL intensity generally characterizes a high recombination rate of the photogenerated charge carrier [51]. The ZnO NDs NBE emission intensity shows a remarkable reduction after coating it with $BiVO_4$. Consequently, it can be stated that the formation of heterojunction between $BiVO_4$ NPs and ZnO NDs can significantly inhibit the recombination rate and decrease the number of crystal defects. The efficiency of charge separation plays a vital role regarding the PEC properties.

UV-vis spectrophotometry was also carried out to study the light absorption capacity of the ZnO electrodes associated with the structural transformation and $BiVO_4$ photosensitization. Absorption and scattering spectra ($A + S = 100 − R − T$) of the samples were calculated by subtracting reflectance (figure 5S(a)) and transmittance (figure 5S(b)) from 100% incident light and illustrated in figure 6(b). Among the electrodes, the most significant non-zero baseline ($\lambda > 400$ nm) was observed for ZnO NDs. The main reason is that the horizontally aligned dense branches surrounding the primary NRs cause scattering. Most photons pass directly through the ITO substrate where they may be internally reflected or escape unmeasured (light loss) [52]. The superior light absorption emerging from structural evolution of the branched ZnO nanostructures was reported previously and justified in a similar way [12, 33]. The spectra also indicate that ZnO NRs and ZnO NDs have very similar UV absorption edges at 380 nm while the absorption edge of

the pure $BiVO_4$ appears at 550 nm. The band gap (E_g) of ZnO NDs and $BiVO_4$ was respectively determined to be 3.2 eV and 2.3 eV through Kubelka–Munk transformation (figure 5S(c)), indicating that the optical response from $BiVO_4$ in the visible region and from ZnO NDs in the UV region effectively contribute to the absorption spectrum of $BiVO_4$/ZnO NDs, manifesting high potential as photoanode with ~55% solar irradiance exploitation capacity.

Figure 6(c) shows the EIS response under illumination in the form of Nyquist plots for all electrodes. The semi-circular arc of the Nyquist plot represents the interfacial charge transfer resistance (R_{ct}), referring to the electron transfer kinetics at the electrode/electrolyte interface. The R_{ct} values were obtained by the equivalent Randle circuit (figure 6(c) inset). The R_{ct} values of ZnO NRs, ZnO NDs, $BiVO_4$ and $BiVO_4$/ZnO NDs were 147, 95, 164 and 52 kΩ, respectively. The branches occupy the void space between the primary NRs and generate more intimate contact at the ZnO NDs electrode/electrolyte interface. The increased electrochemically active surface area results in a relatively lower R_{ct} of ZnO NDs as compared to ZnO NRs. Correlating with PL analysis, these results also confirm that the $BiVO_4$/ZnO NDs heterostructure has the most rapid charge transfer with the lowest resistance, which is desirable for efficient PEC performance. EIS results measured both under dark and illuminated conditions are shown in the supporting information (figure 6S) and indicate the semiconducting nature of the photoelectrode samples upon illumination.

MS analysis was carried out to analyze the intrinsic electronic structures of the $BiVO_4$ and ZnO NDs by measuring the space charge capacitance of the semiconductors at various applied potentials. The slope and the intercept to the *x*-axis of MS plots gives the donor density (N_D) and the flat band potential (V_{fb}) according to equation:

$$\frac{1}{C_s^2} = \frac{2}{e\varepsilon_r\varepsilon_0 N_d A^2}\left(V_{app} - V_{fb} - \frac{kT}{e}\right) \quad (4)$$

where C_s, e, ε_r, ε_0, A, V_{app}, k and T are the space charge layer capacitance, the elementary electric charge, the dielectric constant of the semiconductors, the permittivity of the vacuum, the surface area of the working electrode, the applied potential, the Boltzmann constant, and the temperature, respectively. As can be seen in figure 6(d), both pristine photoelectrodes are the *n*-type semiconductors with positive slopes in the MS plots. The V_{fb} of ZnO NDs was estimated to be 0.123 V (vs NHE at pH 7) or −0.077 V (vs Ag/AgCl). The V_{fb} of $BiVO_4$ was estimated to be −0.070 V (vs NHE at pH 7) or −0.270 V (vs Ag/AgCl). The V_{fb} for $BiVO_4$ lies between −0.7 V and −0.3 V (vs Ag/AgCl) in a pH range of 5.8–7 while the V_{fb} for ZnO lies between −0.29 V and −0.2 V (vs Ag/AgCl) at pH 7.4 [53]. In our study, both estimated V_{fb} values under almost identical conditions are in a good agreement with those reported in the literature. The N_D of ZnO NDs and $BiVO_4$ was estimated to be 0.18×10^{20} (cm^{-3}) and 0.91×10^{19} (cm^{-3}), respectively. It should be emphasized that N_D values deduced from MS plots do not correspond to the absolute concentration as the model is proposed for the planar system [54]. However, this analysis

could signify a qualitative trend in donor density and flat band potential values of the studied semiconductors. Besides, these values strongly depend on the measurement conditions such as the frequency and the pH of electrolyte solution.

The conduction band maxima (E_{CBM}) and the valence band minima (E_{VBM}) of the two semiconductors in the heterostructure were also calculated by the following equations:

$$E_{CBM} = E_F - kT\ln\left(\frac{N_D}{N_C}\right) \text{ and } E_{VBM} = E_{CBM} - E_g. \quad (5)$$

Here, $E_F = -eV_{fb}$ is the Fermi level and $N_C = \left(\frac{2m_h^* kT}{h^2}\right)^{3/2}$ is the effective density of states in the conduction band where $m_h^* = 0.24\ m_0$ for ZnO [55] and $m_h^* = 0.28\ m_0$ for $BiVO_4$ [56]. The exact position of the band edges is specified with respect to the vacuum level on the energy scale. The NHE is located at −4.5 eV (at 298.15 K) compared to the vacuum level. Accordingly, the E_{CBM} and the E_{VBM} of the ZnO NDs were found to lie at −7.57 eV and −4.37 eV (vs vacuum at pH 7), respectively. On the other hand, the E_{CBM} and the E_{VBM} of the $BiVO_4$ were measured to be −6.67 eV and −4.10 eV (vs vacuum at pH 7), respectively. These values are comparable to the previously reported values for ZnO [57] and $BiVO_4$ [58] photoanodes. Considering the fundamentals of heterojunction formation, it is inferred that the $BiVO_4$/ZnO NDs form a typical staggered alignment (type-II heterojunction) [59], suggesting the viability of the electrons transfer from $BiVO_4$ to ZnO.

Figure 7(a) shows the linear sweep voltammetry curves of ZnO NRs, ZnO NDs, $BiVO_4$ and $BiVO_4$/ZnO NDs photoanode samples under AM 1.5 G illumination (87.5 mW·cm^{-2}), including the dark scan. A negligible photocurrent density was observed during the dark scan. The photocurrent of ZnO NRs reached saturation around 0.5 V while the photocurrent of pristine $BiVO_4$ continuously increased with increasing applied potential. ZnO NDs and $BiVO_4$/ZnO NDs photoanodes exhibited almost similar *I–V* characteristics, which partially saturated around 0.7 V but still moderately continued increasing with increasing applied potential. This relatively higher saturated photocurrent was associated with the improved charge transport (lower charge transfer resistance) within the $BiVO_4$/ZnO NDs hybrid anode through branches as direct pathways for photogenerated holes towards electrolyte [60, 61]. At 1.2 V vs NHE, the photocurrent density of the $BiVO_4$/ZnO NDs, ZnO NDs, $BiVO_4$, and ZnO NRs photoanodes are respectively 0.15, 0.10, 0.06, 0.03 mA·cm^{-2}. The improved photocurrent density of ZnO NDs compared to ZnO NRs is associated with its large surface area. Among all the photoanodes, $BiVO_4$/ZnO NDs heterojunction photoanode prepared using the two-step electrodeposition procedure for the formation of $BiVO_4$ nanoislands demonstrated the highest photocurrent density. As indicated by the used characterization studies, the observed significant enhancement in PEC efficiency is attributed to the following factors: the extended light absorption due to narrow band gap $BiVO_4$ sensitization; the
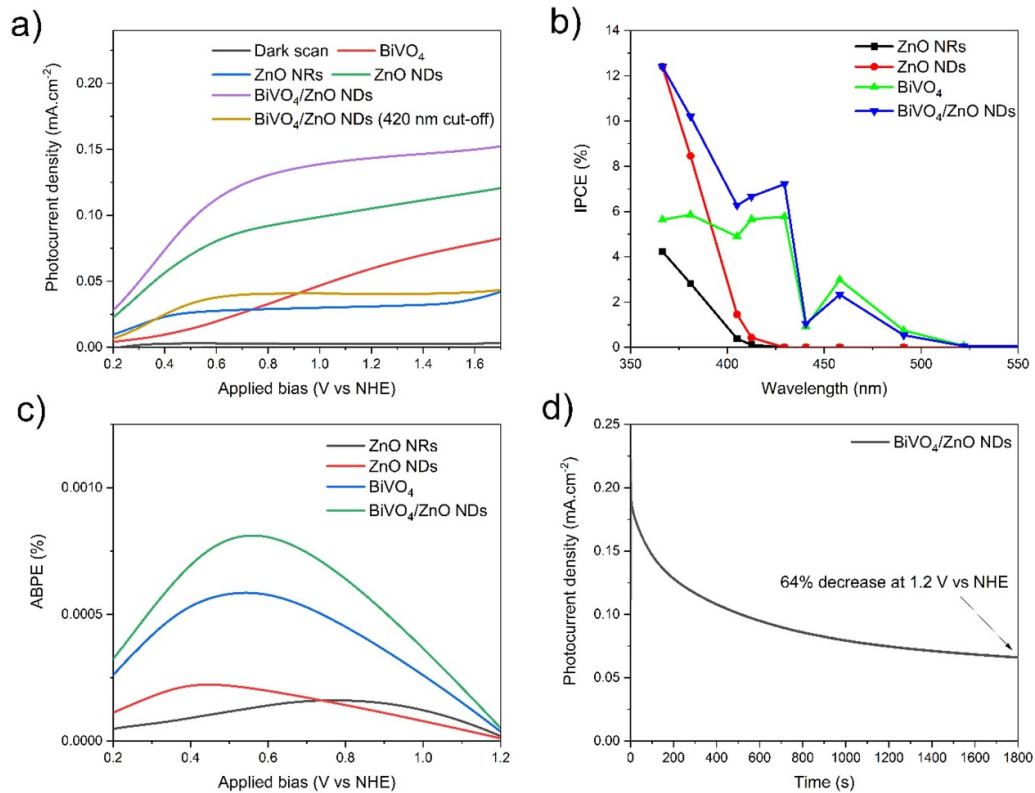
Figure 7. (a) LSV curves, (b) IPCE spectra measured at 1.2 V vs NHE and (c) ABPE spectra of the different photoanodes; and (d) photostability measurement of BiVO$_4$/ZnO NDs heterojunction photoanode at an applied bias of 1.2 V vs NHE.

inhibition of charge recombination after heterojunction formation; the improved charge transfer/transportation as a result of ZnO morphological evolution from NRs to NDs.

To investigate the PEC activity in the visible light, the LSV curve of the BiVO$_4$/ZnO NDs was also recorded under AM 1.5 G irradiation with a UV filter with a 420 nm cut-off wavelength. As presented in figure 7(a), the photocurrent density of BiVO$_4$/ZnO NDs without contribution from UV region is 0.145 mA·cm^{-2}. This also supports the hypothesis that favorable electron transfer from the conduction band of BiVO$_4$ to conduction band of ZnO NDs occurs via visible light absorption.

The IPCE spectra was measured at 1.2 V vs. NHE to elucidate the spectral light response of BiVO$_4$/ZnO NDs heterojunction as compared to pristine BiVO$_4$, ZnO NRs, and ZnO NDs, as shown in figure 7(b). In the UV region, the IPCE of ZnO NDs was up to 12%, which was two and three times higher than those of BiVO$_4$ (6%) and ZnO NRs (4%), respectively. In line with the optical absorption spectra, the IPCE of both ZnO electrodes around 400 nm is almost zero, whereas the IPCE of BiVO$_4$ extended up to 520 nm. The BiVO$_4$/ZnO NDs yielded broadband photoresponse from 360 nm to 520 nm as a result of the coupling narrow band gap of BiVO$_4$ with the wide band gap of ZnO. The ABPE spectra of the produced photoanodes calculated from I–V curves (figure 7(c)) are plotted in figure 7(c). The BiVO$_4$/ZnO NDs heterostructure displayed the highest ABPE, which is about 1.5, 3.6 and 5 times higher

than those of ZnO NDs, BiVO$_4$, and ZnO NDs, respectively. The maximum ABPE was achieved at the potentials of 0.55, 0.53, 0.43, and 0.80 for BiVO$_4$/ZnO NDs, ZnO NDs, ZnO NRs, and BiVO$_4$, respectively. The IPCE and ABPE results are in good agreement with the PEC performance ranking of the fabricated electrodes, suggesting that the practical Faradaic efficiency for H$_2$ evolution for the heterojunction would also be markedly enhanced.

The photostability curve of BiVO$_4$/ZnO NDs heterojunction for a period of 30 min is given in figure 7(d). The photocurrent density of the photoelectrode decreased by 56% in 900 s. In the rest of the curve, the photocurrent density reduction was further reduced by 8% with a relatively more stable behavior and reached totally up to 64% under irradiation at an applied potential of 1.2 V vs NHE in 0.5 M Na$_2$SO$_4$. To gain further insight into the reason of the significant reduction in the photocurrent, SEM image of BiVO$_4$/ZnO NDs photoanode after photostability test is displayed in figure 8. It is interesting to realize that the primarily grown ZnO NRs became severely thinner after 30 min due to the fast degradation in alkaline solution. It is also clearly shown that several parts of the hybrid thin film are missing because of complete separation of ZnO NRs from seed layer on ITO substrate, leading to the formation of regional cavities. Compared to SEM image before the PEC measurements (figure 4(d)), BiVO$_4$ NPs retained their structural integrity to some extent but already appear smaller and discrete on ZnO NDs after 30 min of continuous operation.
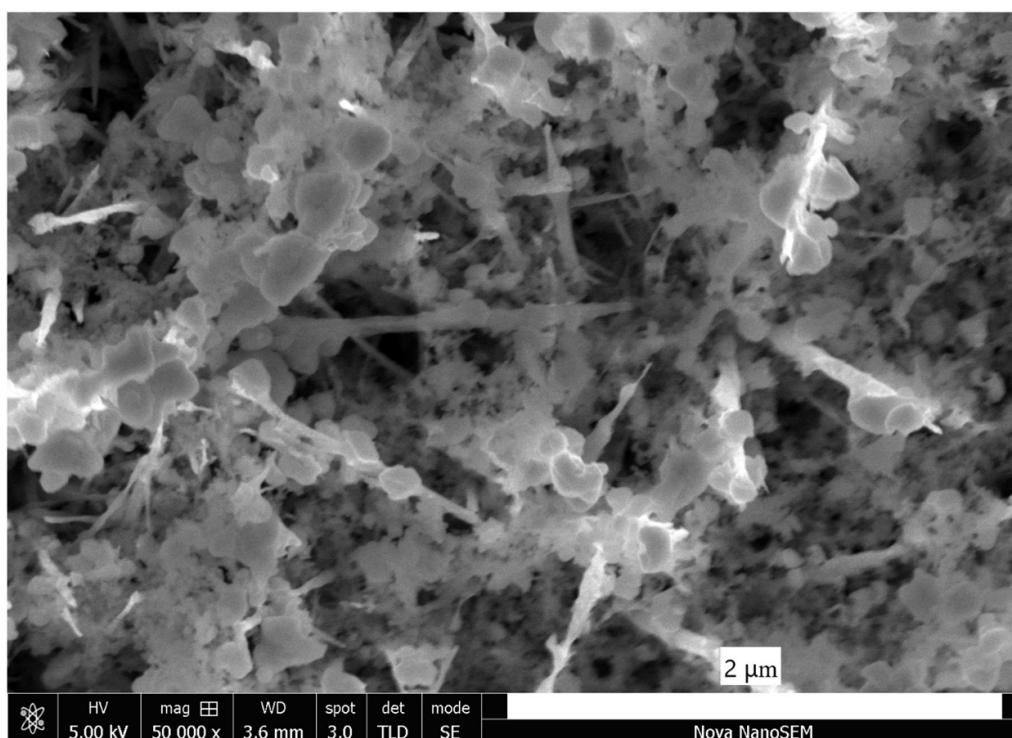
Figure 8. SEM image of BiVO$_4$/ZnO NDs after the photostability test for 30 min under AM 1.5 G illumination at 1.2 V vs NHE.

However, they were observed to be more resilient to corrosion than ZnO. As a result, most of the reduction in photocurrent was determined to be majorly associated with the removal of ZnO NDs from ITO and the partial solvation of BiVO$_4$ NPs in the electrolyte solution, which is taking advantage of the visible light of the solar irradiation. A similar photocorrosion response of BiVO$_4$ coated ZnO NRs operated under almost same conditions (at 1.2 V vs Ag/AgCl in 0.5 M Na$_2$SO$_4$) was reported by Yan *et al* [25].

The schematic energy diagram of the band alignment of the BiVO$_4$/ZnO NDs heterojunction with the PEC mechanism is proposed according to the estimation of band edges of BiVO$_4$ and ZnO NDs (from Mott–Schottky and optical absorption measurements) in scheme 2. Upon AM 1.5 G irradiation, the photogenerated electrons in the CB of BiVO$_4$ flow through the CB of the ZnO, because the CB of BiVO$_4$ was found to lie at a more negative potential (relative to the vacuum) than the CB of ZnO. The accumulated electrons at the CB of the ZnO NDs are then pulled towards the Pt electrode through the conductive ITO substrate to drive the HER. In the meantime, the photogenerated holes at the VB of ZnO migrate and accumulate at the VB of BiVO$_4$ to drive the OER. It is worth noting that ZnO NDs are still in contact with the electrolyte solution (figure 4(d)): a majority of the energetic photogenerated holes are thus likely extracted for OER. Overall, the type-II staggered alignment within BiVO$_4$/ZnO NDs heterojunction stems from the VB of BiVO$_4$ with high density of accumulated holes and the CB of ZnO NDs with high density of accumulated electrons. As confirmed by PL and EIS

studies, this band edge arrangement can remarkably promote the charge separation (low recombination rate) and the interfacial charge transfer/transportation, which lead to the efficient PEC performance for the novel BiVO$_4$ electrodeposited ZnO NDs.

Table 1 shows a comparison of photocurrent for various BiVO$_4$/ZnO photoelectrodes prepared in previous reports. Several studies revealed that BiVO$_4$/ZnO nanostructures achieve better PEC response compared to the pristine form of the constituent semiconductors [62, 63]. The reported photocurrent values in the literature are varying in a wide range from 0.07 mA·cm^{-2} [64] to 1.72 mA·cm^{-2} [25] depending on the used modification method. The majority of the tabulated heterostructures [5, 26, 27] with relatively higher photocurrent values have also been modified by the Co-Pi co-catalyst, which efficiently suppresses surface charge recombination and leads to higher photocurrent density. A systematic analogy of the values obtained in our work with the other values in the literature where AM 1.5 G irradiation was employed in measurements is not very evidentiary because of the inaccuracy of the simulated solar irradiance, particularly at the wavelengths below 365 nm [65], and the not common use of experimental conditions such as electrolyte solution. In this work, BiVO$_4$ nanoislands nested in ZnO NDs with primary NRs diameter of 84 nm and branch length of 300–400 nm was prepared without any co-catalyst modification. The PEC performance of the produced samples have been tested in a home-made PEC cell. BiVO$_4$/ZnO nanocomposite photoanode generated a reproducable higher photocurrent than the

J. Phys. D: Appl. Phys. **57** (2024) 355110

A C Güler *et al*
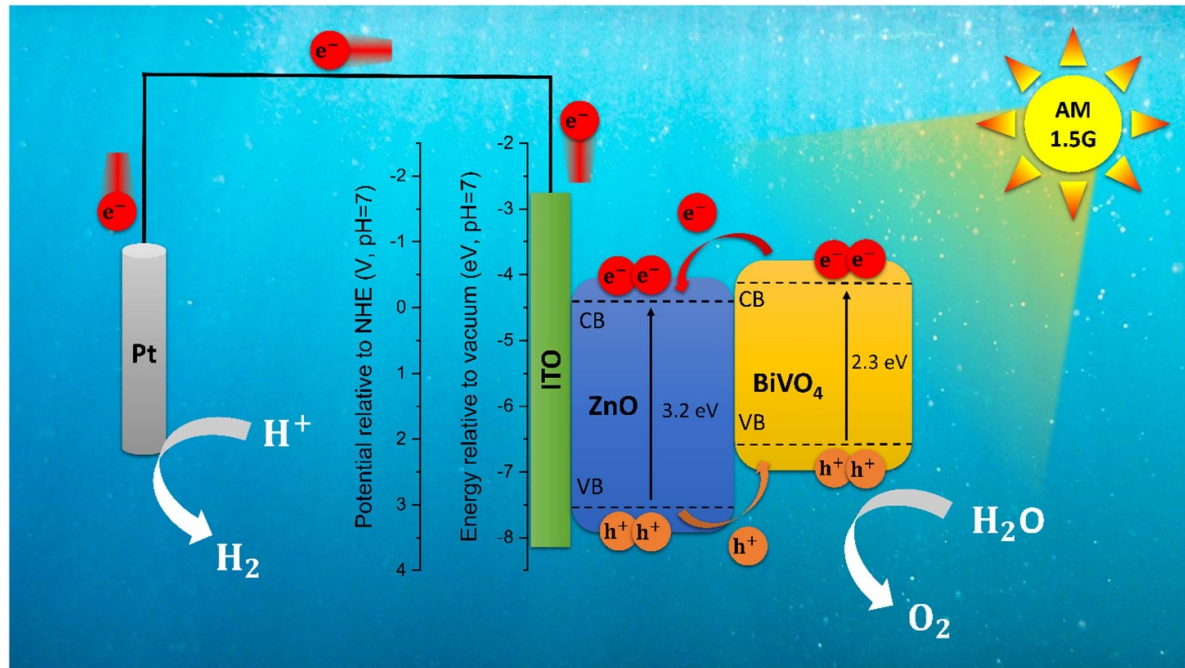
Scheme 2. The estimated band edge alignment within BiVO$_4$/ZnO NDs heterojunction photoanode indicating feasible charge transfer and PEC mechanism under AM 1.5 G illumination.

Table 1. Comparison of the PEC performance of BiVO$_4$/ZnO nanostructured photoanodes modified by different methods.

Heterojunction Photoanode and Ref.	Modification method	Light source	Electrolyte	Photocurrent density
CoPi/BiVO$_4$/ZnO nanodendrites [27]	Metal organic decomposition	AM1.5 g simulated sunlight at 100 mW·cm^{-2}	0.3 M Na$_2$SO$_4$ with potassium phosphate at pH 7.5	3.5 mA·cm^{-2} at 1.23 V vs RHE
1D-ZnO nanorods/ BiVO$_4$ [64]	Wet chemical reaction	A 150 W Xe light at 100 mW·cm^{-2}	0.5 M Na$_2$SO$_4$ at pH 7	0.07 mA·cm^{-2} at 0.2 V vs Ag/AgCl
Dual layer BiVO$_4$/ZnO [53]	Co-precipitation	Xe lamp with AM1.5 at 100 mW·cm^{-2}	1 M NaOH	3.5 mA·cm^{-2} at 1.2 V vs RHE
1D ZnO/BiVO4 [25]	Silar	Xe lamp at 100 mW·cm^{-2}	0.5 M Na$_2$SO$_4$	1.72 mA·cm^{-2} at 1.2 V vs Ag/AgCl
3D-Bicontinuous BiVO$_4$/ZnO with CoPi [5]	Metal organic decomposition	Xe lamp with AM1.5	0.2 M Na$_2$SO$_4$ at pH 6.5	3.4 mA·cm^{-2} at 0.6 V vs RHE
1D Co-Pi Modifi ed BiVO$_4$/ZnO [26]	Spray pyrolysis	Xenon lamp at 75 mW·cm^{-2}	0.5 M Na$_2$SO$_4$	3 mA·cm^{-2} at 1.2 V vs RHE
In this study	Electrodeposition	Solar simulator with AM1.5 g at 87.5 mW·cm^{-2}	0.5 M Na$_2$SO$_4$	0.15 mA·cm^{-2} at 1.2 V vs NHE

other produced electrodes. The use of electrodeposition facilitates a good control over the deposition thickness and deposit characteristics. Nevertheless, the major obstacle in producing Bi layer by electroplating solution is the insolubility of the Bi(III) salts unless the solution is strongly acidic. The semiconductor of interest to form heterojunction with BiVO$_4$ must be robust in strong acidic aqueous solutions. Therefore, further research activities are needed to develop moderate conditions for electrodeposition of Bi metal on ZnO NDs to ensure maximum sunlight utilization during PEC water splitting.

4. Conclusion

In summary, the BiVO$_4$/ZnO NDs nanostructure was successfully produced via a facile combination of hydrothermal method without secondary seed layer and Bi metal film electrodeposition followed by the introduction of V precursor solution and thermal treatment. The Bi deposition on ZnO NDs with good adhesion and coverage was achieved after 5 min at −1 V vs. Ag/AgCl electrode. Through flat band and optical measurements, it was determined that BiVO$_4$/ZnO NDs have type II band alignment, allowing photogenerated electron

J. Phys. D: Appl. Phys. **57** (2024) 355110

A C Güler *et al*

transfer from BiVO$_4$ to ZnO, and vice versa for photogenerated holes. As a result, the BiVO$_4$/ZnO heterojunction photoanode exhibited the highest photocurrent (0.15 mA·cm^{-2} at 1.2 V vs. NHE), which is 1.5, 2.5 and 5 times higher than that of ZnO NDs, BiVO$_4$, ZnO NRs photoanodes produced in this study. The significant advancement in photocurrent efficiency of the heterojunction photoanode produced in this study was associated with several factors: (1) enhanced light absorption towards the visible light region (due to narrow band gap of 2.3 eV for BiVO$_4$); (2) favorable charge transfer confirmed by lower interfacial charge transfer resistance (thinner branches around NRs endows larger contact area between electrode/electrolyte); (3) suppression of charge recombination rate, thus more efficient charge separation. The electrodeposition of primary metal layer to convert into visible light absorber material is a feasible approach to sensitize photoanode materials with poor light absorption. On this basis, the current work can be expanded to fabricate various highly efficient heterostructured photoanodes for use in PEC water splitting and other solar energy applications.

Data availability statement

All data that support the findings of this study are included within the article (and any supplementary files).

Acknowledgments

Conflict of interest

The authors declare no conflict of interest.

ORCID iD

Ivo Kuřitka https://orcid.org/0000-0002-1016-5170

References

[1] Jia J, Seitz L C, Benck J D, Huo Y, Chen Y, Ng J W D, Bilir T, Harris J S and Jaramillo T F 2016 Solar water splitting by photovoltaic-electrolysis with a solar-to-hydrogen efficiency over 30% *Nat. Commun.* **7** 1–6

[2] Fujishima A and Honda K 1972 Electrochemical photolysis of water at a semiconductor electrode *Nature* **238** 37–38

[3] Marwat M A *et al* 2021 Advanced catalysts for photoelectrochemical water splitting *ACS Appl. Energy Mater.* **4** 12007–31

[4] Li D, Shi J and Li C 2018 Transition-metal-based electrocatalysts as cocatalysts for photoelectrochemical water splitting: a mini review *Small* **14** 1–22

[5] Kim K and Moon J H 2018 Three-dimensional bicontinuous BiVO$_4$/ZnO photoanodes for high solar water-splitting performance at low bias potential *ACS Appl. Mater. Interfaces* **10** 34238–44

[6] Tang J, Durrant J R and Klug D R 2008 Mechanism of photocatalytic water splitting in TiO$_2$. Reaction of water with photoholes, importance of charge carrier dynamics, and evidence for four-hole chemistry *J. Am. Chem. Soc.* **130** 13885–91

[7] Ma M, Huang Y, Liu J, Liu K, Wang Z, Zhao C, Qu S and Wang Z 2020 Engineering the photoelectrochemical behaviors of ZnO for efficient solar water splitting *J. Semicond.* **41** 091702

[8] Hochbaum A I and Yang P 2016 Semiconductor nanowires for energy harvesting *Semicond. Semimet.* **94** 297–368

[9] Law M, Goldberger J and Yang P 2004 Semiconductor nanowires and nanotubes *Annu. Rev. Mater. Res.* **34** 83–122

[10] Song X M, Wu J M, Tang M Z, Qi B and Yan M 2008 Enhanced photoelectrochemical response of a composite titania thin film with single-crystalline rutile nanorods embedded in anatase aggregates *J. Phys. Chem. C* **112** 19484–93

[11] Berglund S P, Abdi F F, Bogdanoff P, Chemseddine A, Friedrich D and Van De Krol R 2016 Comprehensive evaluation of CuBi$_2$O$_4$ as a photocathode material for photoelectrochemical water splitting *Chem. Mater.* **28** 4231–42

[12] Bai Z, Yan X, Li Y, Kang Z, Cao S and Zhang Y 2016 3D-branched ZnO/CdS nanowire arrays for solar water splitting and the service safety research *Adv. Energy Mater.* **6** 1–8

[13] Jiang C Y, Sun X W, Lo G Q, Kwong D L and Wang J X 2007 Improved dye-sensitized solar cells with a ZnO-nanoflower photoanode *Appl. Phys. Lett.* **90** 3–6

[14] Li Q, Sun X, Lozano K and Mao Y 2016 Dependence of photoelectrochemical properties on geometry factors of interconnected "Caterpillar-like" ZnO networks *Electrochim. Acta* **222** 232–45

[15] Ko S H, Lee D, Kang H W, Nam K H, Yeo J Y, Hong S J, Grigoropoulos C P and Sung H J 2011 Nanoforest of hydrothermally grown hierarchical ZnO nanowires for a high efficiency dye-sensitized solar cell *Nano Lett.* **11** 666–71

[16] Li X, Niu F, Su J and Guo L 2018 Photoelectrochemical performance dependence on geometric surface area of branched ZnO nanowires *ChemElectroChem* **5** 3717–22

[17] Sounart T L, Liu J, Voigt J A, Hsu J W P, Spoerke E D, Tian Z and Jiang Y 2006 Sequential nucleation and growth of complex nanostructured films *Adv. Funct. Mater.* **16** 335–44

[18] Wu C T, Liao W P and Wu J J 2011 Three-dimensional ZnO nanodendrite/nanoparticle composite solar cells *J. Mater. Chem.* **21** 2871–6

[19] Bai Y, Lu J, Bai H, Fang Z, Wang F, Liu Y, Sun D, Luo B, Fan W and Shi W 2021 Understanding the key role of vanadium in p-type BiVO$_4$ for photoelectrochemical N$_2$ fixation *Chem. Eng. J.* **414** 128773

[20] García-Pérez U M, Sepúlveda-Guzmán S and Martínez-De La Cruz A 2012 Nanostructured BiVO$_4$ photocatalysts synthesized via a polymer-assisted coprecipitation method and their photocatalytic properties under visible-light irradiation *Solid State Sci.* **14** 293–8

[21] Kudo A, Omori K and Kato H 1999 A novel aqueous process for preparation of crystal form-controlled and highly

J. Phys. D: Appl. Phys. **57** (2024) 355110

A C Güler *et al*

crystalline BiVO$_4$ powder from layered vanadates at room temperature and its photocatalytic and photophysical properties *J. Am. Chem. Soc.* **121** 11459–67

[22] Yu J and Kudo A 2006 Effects of structural variation on the photocatalytic performance of hydrothermally synthesized BiVO$_4$. *Adv. Funct. Mater.* **16** 2163–9

[23] Wang H T *et al* 2021 Role of interfacial defects in photoelectrochemical properties of BiVO$_4$ coated on ZnO nanodendrites: x-ray spectroscopic and microscopic investigation *ACS Appl. Mater. Interfaces* **13** 41524–36

[24] Li S, Xu W, Meng L, Tian W and Li L 2022 Recent progress on semiconductor heterojunction-based photoanodes for photoelectrochemical water splitting *Small Sci.* **2** 2100112

[25] Yan L, Zhao W and Liu Z 2016 1D ZnO/BiVO$_4$ heterojunction photoanodes for efficient photoelectrochemical water splitting *Dalton Trans.* **45** 11346–52

[26] Moniz S J A, Zhu J and Tang J 2014 1D Co-Pi modified BiVO$_4$/ZnO junction cascade for efficient photoelectrochemical water cleavage *Adv. Energy Mater.* **4** 1–8

[27] Yang J and Wu J 2017 Low-potential driven fully-depleted BiVO$_4$/ZnO heterojunction nanodendrite array photoanodes for photoelectrochemical water splitting *Nano Energy* **32** 232–40

[28] Kim T W and Choi K S 2014 Nanoporous BiVO$_4$ photoanodes with dual-layer oxygen evolution catalysts for solar water splitting *Science* **343** 990–4

[29] Kang D, Park Y, Hill J C and Choi K 2014 Preparation of Bi-based ternary oxide photoanodes BiVO$_4$, Bi$_2$WO$_6$, and Bi$_2$Mo$_3$O$_{12}$ using dendritic Bi metal electrodes *J. Phys. Chem. Lett.* **5** 2994–9

[30] Bai S, Liu J, Cui M, Luo R, He J and Chen A 2018 Two-step electrodeposition to fabricate the p-n heterojunction of a Cu$_2$O/BiVO$_4$ photoanode for the enhancement of photoelectrochemical water splitting *Dalton Trans.* **47** 6763–71

[31] Wu C T and Wu J J 2011 Room-temperature synthesis of hierarchical nanostructures on ZnO nanowire anodes for dye-sensitized solar cells *J. Mater. Chem.* **21** 13605–10

[32] Zarębska K, Kwiatkowski M, Gniadek M and Skompska M 2013 Electrodeposition of Zn(OH)$_2$, ZnO thin films and nanosheet-like Zn seed layers and influence of their morphology on the growth of ZnO nanorods *Electrochim. Acta* **98** 255–62

[33] Sun X, Li Q, Jiang J and Mao Y 2014 Morphology-tunable synthesis of ZnO nanoforest and its photoelectrochemical performance *Nanoscale* **6** 8769–80

[34] Dhas C R, Arivukarasan D, Venkatesh R, Josephine A J, Gnana Malar K C M, Santhoshi Monica S E and Subramanian B 2019 Influence of precursor aging time period on physical and photocatalytic properties of nebulizer spray coated BiVO$_4$ thin films *Solid State Sci.* **92** 36–45

[35] Vieira N C S, Fernandes E G R, De Queiroz A A A, Guimarães F E G and Zucolotto V 2013 Indium tin oxide synthesized by a low cost route as SEGFET pH sensor *Mater. Res.* **16** 1156–60

[36] Dias L P, Correia F C, Ribeiro J M and Tavares C J 2020 Photocatalytic Bi$_2$O$_3$/TiO$_2$:N thin films with enhanced surface area and visible light activity *Coatings* **10** 445

[37] Montenegro D N, Hortelano V, Martínez O, Martínez-Tomas M C, Sallet V, Muñoz-Sanjosé V and Jiménez J 2013 Non-radiative recombination centres in catalyst-free ZnO nanorods grown by atmospheric-metal organic chemical vapour deposition *J. Phys. D: Appl. Phys.* **46** 235302

[38] Hermans Y, Klein A, Ellmer K, Van De Krol R, Toupance T and Jaegermann W 2018 Energy-band alignment of BiVO$_4$ from photoelectron spectroscopy of solid-state interfaces *J. Phys. Chem. C* **122** 20861–70

[39] Thalluri S R M, Martinez-Suarez C, Virga A, Russo N and Saracco G 2013 Insights from crystal size and band gap on the catalytic activity of monoclinic BiVO$_4$ *Int. J. Chem. Eng. Appl.* **4** 305–9

[40] Sahai A and Goswami N 2015 Structural and optical investigations of oxygen defects in zinc oxide nanoparticles *AIP Conf. Proc.* **1665** 050023

[41] Palaniselvam T, Shi L, Mettela G, Anjum D H, Li R, Katuri K P, Saikaly P E and Wang P 2017 Vastly enhanced BiVO$_4$ photocatalytic OER performance by NiCoO$_2$ as cocatalyst *Adv. Mater. Interfaces* **4** 1–10

[42] Mali S S, Park G R, Kim H, Kim H H, Patil J V and Hong C K 2019 Synthesis of nanoporous Mo:BiVO$_4$ thin film photoanodes using the ultrasonic spray technique for visible-light water splitting *Nanoscale Adv.* **1** 799–806

[43] Cossuet T, Donatini F, Lord A M, Appert E, Pernot J and Consonni V 2018 Polarity-dependent high electrical conductivity of ZnO nanorods and its relation to hydrogen *J. Phys. Chem. C* **122** 22767–75

[44] Granqvist C G and Hultåker A 2002 Transparent and conducting ITO films: new developments and applications *Thin Solid Films* **411** 1–5

[45] Mistry A and Srinivasan V 2019 On our limited understanding of electrodeposition *MRS Adv.* **4** 2843–61

[46] Wang Y, Wang Q, Zhan X, Wang F, Safdar M and He J 2013 Visible light driven type II heterostructures and their enhanced photocatalysis properties: a review *Nanoscale* **5** 8326–39

[47] Li W, Wang G, Chen C, Liao J and Li Z 2017 Enhanced visible light photocatalytic activity of ZnO nanowires doped with Mn^{2+} and Co^{2+} ions *Nanomaterials* **7** 1–11

[48] Feng J, Cheng L, Zhang J, Okoth O K and Chen F 2018 Preparation of BiVO$_4$/ZnO composite film with enhanced visible-light photoelectrocatalytic activity *Ceram. Int.* **44** 3672–7

[49] Raji R and Gopchandran K G 2017 ZnO nanostructures with tunable visible luminescence: effects of kinetics of chemical reduction and annealing *J. Sci. Adv. Mater. Dev.* **2** 51–58

[50] Pham V T, Dao B T T, Nguyen H T T, Tran N Q, Le Hang D T, Trung N D, Lee T, Bach L G and Nguyen T D 2022 Substitution of V^{5+} in BiVO$_4$ with Ni^{2+} and the improved photocatalytic degradation of crystal violet under white LED light irradiation *Top. Catal.* **66** 2–11

[51] Kadam A N, Lee J, Nipane S V and Lee S W 2021 *Nanocomposites for Visible Light Photocatalysis* vol 3 (Elsevier Inc.)

[52] Cho I S, Chen Z, Forman A J, Kim D R, Rao P M, Jaramillo T F and Zheng X 2011 Branched TiO$_2$ nanorods for photoelectrochemical hydrogen production *Nano Lett.* **11** 4978–84

[53] Singh S, Ruhela A, Rani S, Khanuja M and Sharma R 2018 Concentration specific and tunable photoresponse of bismuth vanadate functionalized hexagonal ZnO nanocrystals based photoanodes for photoelectrochemical application *Solid State Sci.* **76** 48–56

[54] Antony R P, Zhang M, Zhou K, Loo S C J, Barber J and Wong L H 2018 Synergistic effect of porosity and gradient doping in efficient solar water oxidation of catalyst-free gradient Mo:BiVO$_4$ *ACS Omega* **3** 2724–34

[55] Rasouli F, Rouhollahi A and Ghahramanifard F 2019 Gradient doping of copper in ZnO nanorod photoanode by electrodeposition for enhanced charge separation in photoelectrochemical water splitting *Superlattices Microstruct.* **125** 177–89

[56] Ullah H, Tahir A A and Mallick T K 2018 Structural and electronic properties of oxygen defective and Se-doped p-type BiVO$_4$(001) thin film for the applications of photocatalysis *Appl. Catal.* B **224** 895–903

J. Phys. D: Appl. Phys. **57** (2024) 355110

A C Güler *et al*

[57] Tzeng L-J, Cheng C-L and Chen Y-F 2008 Enhancement of band-edge emission induced by defect transition in the composite of ZnO nanorods and CdSe/ZnS quantum dots *Opt. Lett.* **33** 569

[58] Kim C W, Ji S, Kang M J, Park H, Li F, Cheng H M and Kang Y S 2019 Energy band edge alignment of anisotropic BiVO$_4$ to drive photoelectrochemical hydrogen evolution *Mater. Today Energy* **13** 205–13

[59] Zheng Z, Zu X, Zhang Y and Zhou W 2020 Rational design of type-II nano-heterojunctions for nanoscale optoelectronics *Mater. Today Phys.* **15** 100262

[60] Selopal G S, Mohammadnezhad M, Navarro-Pardo F, Vidal F, Zhao H, Wang Z M and Rosei F 2019 A colloidal heterostructured quantum dot sensitized carbon nanotube-TiO$_2$ hybrid photoanode for high efficiency hydrogen generation *Nanoscale Horiz.* **4** 404–14

[61] Guler A C, Antos J, Masar M, Machovsky M, Kuritka I and Urbanek M 2023 Comprehensive evaluation of photoelectrochemical performance dependence on geometric features of ZnO nanorod electrodes † *Nanoscale Adv.* **5** 3091–103

[62] He X, Tian W, Bai Z, Yang L and Li L 2022 Decoration of BiVO$_4$/ZnO photoanodes with Fe-ZIF-8 to simultaneously enhance charge separation and hole transportation for efficient solar water splitting *ChemPhotoChem* **6** e202200113

[63] Hou H, Liu H, Gao F, Shang M, Wang L, Xu L, Wong W Y and Yang W 2018 Packaging BiVO$_4$ nanoparticles in ZnO microbelts for efficient photoelectrochemical hydrogen production *Electrochim. Acta* **283** 497–508

[64] Chang J S, Phuan Y W, Chong M N and Ocon J D 2020 Exploration of a novel Type II 1D-ZnO nanorods/BiVO$_4$ heterojunction photocatalyst for water depollution *J. Ind. Eng. Chem.* **83** 303–14

[65] Govatsi K, Seferlis A, Neophytides S G and Yannopoulos S N 2018 Influence of the morphology of ZnO nanowires on the photoelectrochemical water splitting efficiency *Int. J. Hydrog. Energy* **43** 4866–79